Mechanisms of Meridional-Propagating High-Frequency Intraseasonal Oscillation Associated with a Persistent Rainfall over South China

BIN ZHENG AND YANYAN HUANG

Guangzhou Institute of Tropical and Marine Meteorology, China Meteorological Administration, and Guangdong Provincial Key Laboratory of Regional Numerical Weather Prediction, Guangzhou, China

(Manuscript received 13 September 2017, in final form 12 March 2018)

ABSTRACT

The present study divides the intraseasonal variations into high-frequency intraseasonal oscillation (HF-ISO) with a 5–20-day period and low-frequency ISO (LF-ISO) with a 30–60-day period. Here, defined HF-ISO is heavily different from some previous work, because, over south China, persistent rainfall (PR) is not only related to the quasi-biweekly oscillation (10–20-day period), but also connected with the quasi-weekly oscillation (5–10-day period). Associated with a PR over south China during the first half of June 2016 (PR1606), the propagating components of the convections are largely attributed to the HF-ISOs. Moreover, both southward- and northward-propagating HF-ISOs are found in this case. Over southern China, the moisture advection dominated by anomalous flow and mean water vapor plays an important role in the southward propagation of the HF-ISO, and the cloud–radiation effect may be also, at least partially, responsible for the southward shift of the associated convective zone. Nevertheless, two other possible mechanisms are introduced to explain the cause of the northward propagation of the HF-ISO over southern China during the PR1606 period. The first is the vorticity advection, which is a dominant factor. The second mechanism is the wind–evaporation effect that plays a minor role. Over the South China Sea, the northward propagation of the HF-ISO is mainly attributed to the vertical wind shear effect and the vorticity advection effect, and the latter is relatively more important than the former in this case. The moisture advection is a supplementary effect caused by inducing a weak positive moisture tendency north of the convection center.

1. Introduction

Persistent rainfall (PR) is one of the most common meteorological disasters in the flood season over southern China, but its predictability is often confined to within one week (Goswami and Xavier 2003; Zhao et al. 2016). Understanding the physical processes associated with the PR is one effective way to improve the predictability.

A PR process needs dynamical conditions first. The formation of positive vorticity anomalies is one important dynamical process. The positive vorticity anomalies related to the PR over southern China can result from the advection by the mean flow (Hong et al. 2015), the southward propagation of the low-frequency oscillations (Hong and Ren 2013), or the eastward propagation of the positive vorticity from the Tibetan Plateau (Li et al. 2014). Moreover, the local vertical nonuniformity of the diabatic heating has an important influence on the vorticity tendency, and the positive vorticity tendency is found over southern China during the PR developing period (Hong et al. 2015). For the PR over southern China, the background circulations also provide dynamic support via the interactions with the eddy flows (Fu et al. 2016; Zhang et al. 2017). The cold air and monsoon are the main background systems that impact the PR over East Asia (Zheng et al. 2007; Li et al. 2014; Imada et al. 2015; Liu et al. 2016). The thermal–dynamical effect of the Tibetan Plateau is commonly considered an important role for the activities of the East Asian monsoon and South China Sea (SCS) summer monsoon (SCSSM; Wan and Wu 2009; Zhang et al. 2013; Li et al. 2014; Huang et al. 2015).

Meanwhile moisture conditions control the PR processes. There are three water vapor pathways associated with the PR over southern China: the tropical Indian Ocean, the SCS, and the western North Pacific (WNP). While different types of the PR over southern China

Denotes content that is immediately available upon publication as open access.

Corresponding author: Bin Zheng, zhb@ustc.edu

DOI: 10.1175/MWR-D-17-0260.1

correspond to the three moisture sources, generally most of the water vapor comes from the WNP for the PR during mid-March to mid-May (viz., the spring rainfall over southern China) (Lin et al. 2013; Lin et al. 2014; Zhang et al. 2015). It is attributed to the increase of the land–sea thermal contrast (Tian and Yasunari 1998; Zhang et al. 2013). Following the onset of the SCSSM, the main source of the water vapor is the SCS from mid-May to late August (Liu et al. 2016), since the seasonal march of the SCSSM or atmospheric circulation over East Asia is along the way from the SCS to southern China (Liao and Tao 2004; Li et al. 2007). When the PR occurs during late July to early October, the moisture is mainly transported from the Indian Ocean and the principal rainfall belts are located to the east of southern China (Liu et al. 2016).

There are close connections between the processes of the PR mentioned above and the low-frequency oscillation (Ren et al. 2013; Li et al. 2015; Hui and Fang 2016a,b; J. Wang et al. 2017), so the regional East Asia–WNP intraseasonal oscillation (ISO) index can be introduced to monitor the persistent heavy rainfall in south China during the early flood season (Gao et al.2016). The ISOs usually include two periods (10–20 and 30–60 days) (Krishnamurthy and Shukla 2007; Li et al. 2015; Hui and Fang2016a,b), and impact the precipitation over southern China with a northward or northwestward movement (Li et al. 2015; Chen et al. 2015; Gao et al. 2016). The mechanisms for northward propagation of ISO mainly include feedbacks from land surface heat fluxes (Webster and Holton 1982), convection–moist stability interaction (Goswami and Shukla 1984), air–sea interaction (Kemball-Cook and Wang 2001), vertical easterly wind shear (Wang and Xie 1997; Jiang et al. 2004; Drbohlav and Wang 2005), cumulus convection (Kang et al. 2010; Liu et al. 2015), and the beta shift (Boos and Kuang 2010). Chou and Hsueh (2010) examined some dominant mechanisms of northward-propagating ISOs with 30–60-day period over the Indian Ocean and the WNP. They include the following: 1) the vorticity advection effect, which is associated with the advection of anomalous baroclinic vorticity by mean baroclinic meridional winds; 2) the vertical wind shear effect, which is the vertical advection associated with the meridional gradient of baroclinic divergence and mean easterly vertical wind shear; 3) the moisture advection effect induced by mean flow; and 4) the air–sea interaction via surface latent heat flux. The PBL moisture advection and barotropic vorticity effect are found to be the dominant mechanisms for the northward propagation (DeMott et al. 2013). In their study, M. Wang et al. (2017) concluded that there are three main mechanisms of the northward-propagating quasi-biweekly oscillation (QBWO): barotropic vorticity, boundary moisture advection, and surface sensible heating (SSH).

Over south China, the PR is not only related to the QBWO, but also connected with the quasi-weekly oscillation (Gu and Zhang 2012; Gu et al. 2013). Thus, in this study, we divide the ISOs over the SCS and southern China into high-frequency ISOs (HF-ISOs) with a 5–20-day period and low-frequency ISOs (LH-ISOs) with a 30–60-day period, and then analyze the effects of the meridional propagations of them on the PR over south China in the first half of June 2016 (PR1606 hereafter). The next section describes the datasets and methods used in this study. Section 3 states the relationship between the propagations of ISOs and the PR1606. A detailed discussion about the propagation mechanisms is presented in section 4, followed by the conclusions from this study.

2. Data and analysis method

a. Data

In this study, most of the data, including winds, water vapor, geopotential height, air temperature, vorticity, divergence, surface fluxes (surface solar radiation, longwave radiation, latent, and sensible heat fluxes), and sea surface/land skin temperature are from the Japanese 55-year Reanalysis (JRA-55; Kobayashi et al. 2015) and the National Centers for Environmental Prediction–National Center for Atmospheric Research (NCEP–NCAR) reanalysis (Kalnay et al. 1996). Positive longwave radiation, latent, and sensible heat fluxes mean that the energy transfers from the ocean/land to the atmosphere and vice versa for negative values, while shortwave radiation is positive when the energy transfers from the atmosphere to the ocean/land. Daily SST and precipitation come from the NOAA optimum interpolation (OI) SST V2 high-resolution dataset (OISST.V2; Reynolds et al. 2007) and the Global Precipitation Climatology Project (GPCP) satellite-derived infrared (IR) GOES precipitation index (GPI) daily rainfall estimates (Huffman et al. 2001), respectively.

b. Analysis method

For convenience, all data are interpolated into $1^\circ \times 1^\circ$ spatial resolution as the GPI daily precipitation. Moreover, all data except for climatological variations were filtered by 5–20- and 30–60-day bandpass filters. The climatological mean is from 1981 to 2010. ISOs are identified by maximum-filtered precipitation anomalies averaged over the longitudes (105°–120°), and divided into high-frequency ISO (HF-ISO) with a 5–20-day

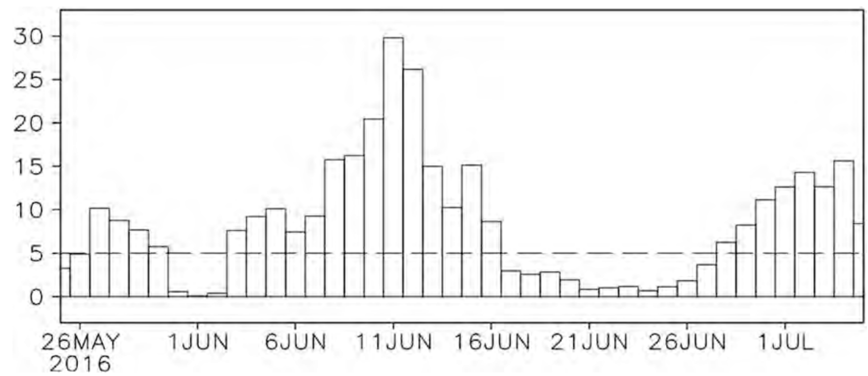

FIG. 1. Time series of daily precipitation over south China. The dashed line denotes 5 mm day^{-1} precipitation.

period and low-frequency ISO (LF-ISO) with a 30–60-day period, which is different from the definition over South Asia by Karmakar et al. (2017). The latitude with maximum zonally averaged precipitation anomalies was chosen as reference latitude (zero latitude) for a composite, which covers 10°N/S latitudes of the reference latitude.

3. A persistent rainfall event in South China

GPI data show that the daily regional precipitation (Fig. 1) over south China (20°–25°N, 105°–120°E) larger than 5 mm was sustained from 3 to 16 June 2016, with the maximum value approaching 30 mm. Obviously, there was a persistent rainfall over south China during the first half of June 2016 (viz., PR1606, shown by the red rectangular boxes with dashed lines in Fig. 2a). Two evident processes can be seen from the mean (Fig. 2a) or anomalies (Fig. 2b) of precipitation. One is a southward propagation of the convections along 105°–120°E before 6 June, and another is a northward propagation from the equatorial region throughout the PR1606 period. Figures 2c and 2d display the LF-ISOs and HF-ISOs for the anomalous precipitation, respectively. The LF-filtered precipitation indicates the positive anomalies almost cover the PR1606 period, but it seems a local phenomenon with few

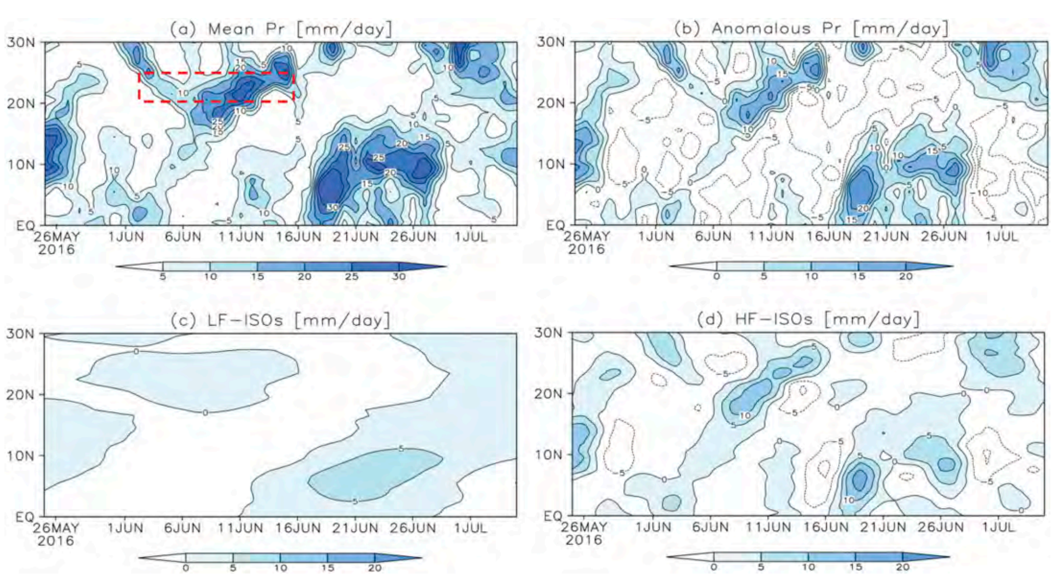

FIG. 2. (a) The 105°–120°E zonal mean of the precipitation, (b) anomalous precipitation, (c) LF-filtered precipitation, and (d) HF-filtered precipitation. The red rectangular box with the dashed line denotes the PR event over south China (PR1606).

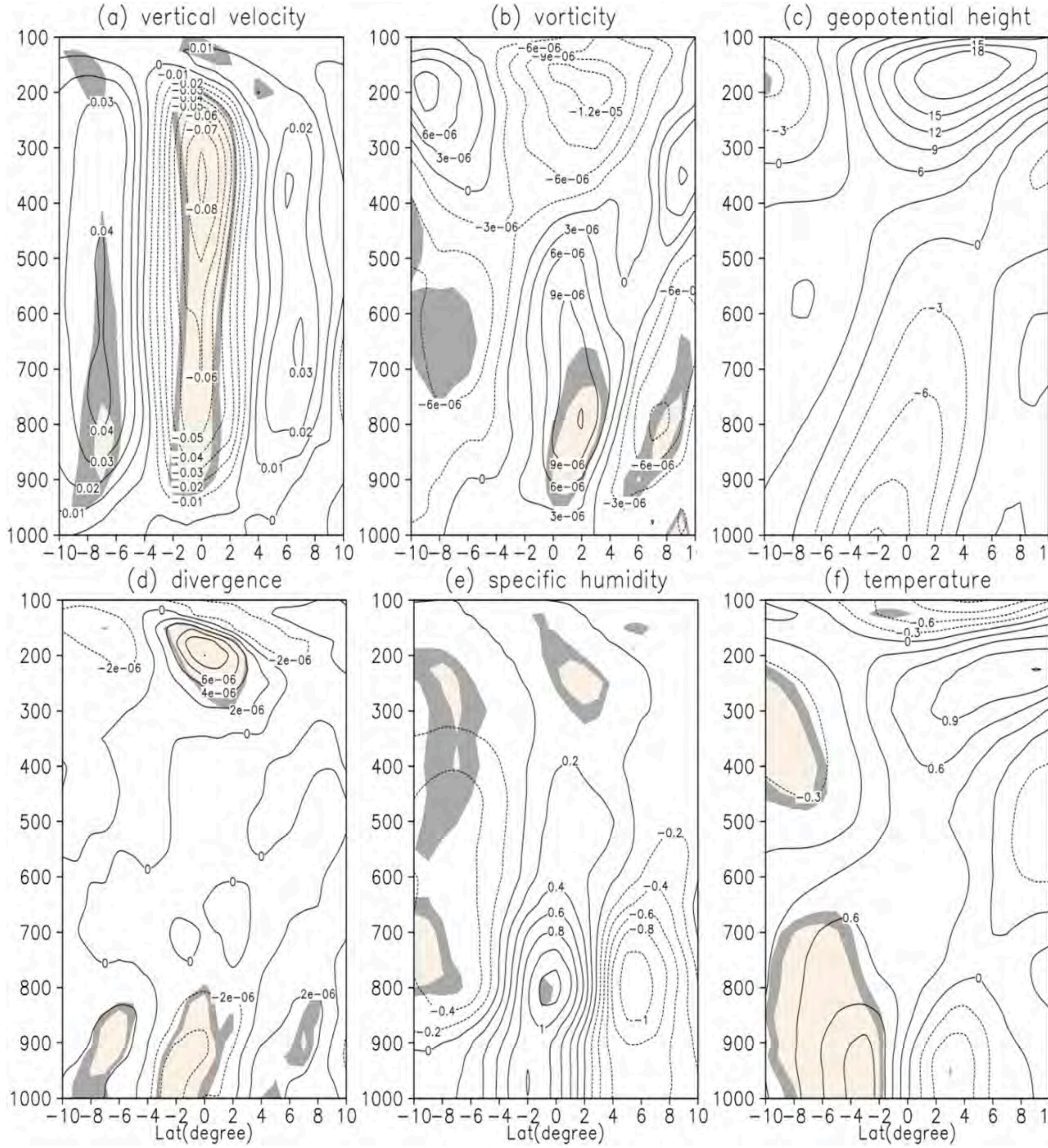

FIG. 3. Composites of the southward-propagating HF-ISO based on the maximum precipitation for (a) vertical velocity (Pa s^{-1}), (b) vorticity (s^{-1}), (c) geopotential height (gpm), (d) divergence (s^{-1}), (e) specific humidity (g kg^{-1}), and (f) air temperature (K) from JRA-55. All variables are after 5–20-day filtering. The positive (negative) value of the x axis means the distance to the north (south) of the convection center. The vertical axis is the pressure (hPa). The two shaded areas indicate the composite anomalies exceeding 90% and 95% confidence levels.

relationships to the meridional-propagating LF-ISO. Nevertheless, the HF-ISOs have similar propagating processes to the mean and anomalous precipitation. It implies the propagating components of the convections can be attributed to the HF-ISOs that impact the PR1606 by their meridional propagation. In this study, we focus on the HF-ISOs to reveal the possible causes of the meridional propagations based on the case of PR1606.

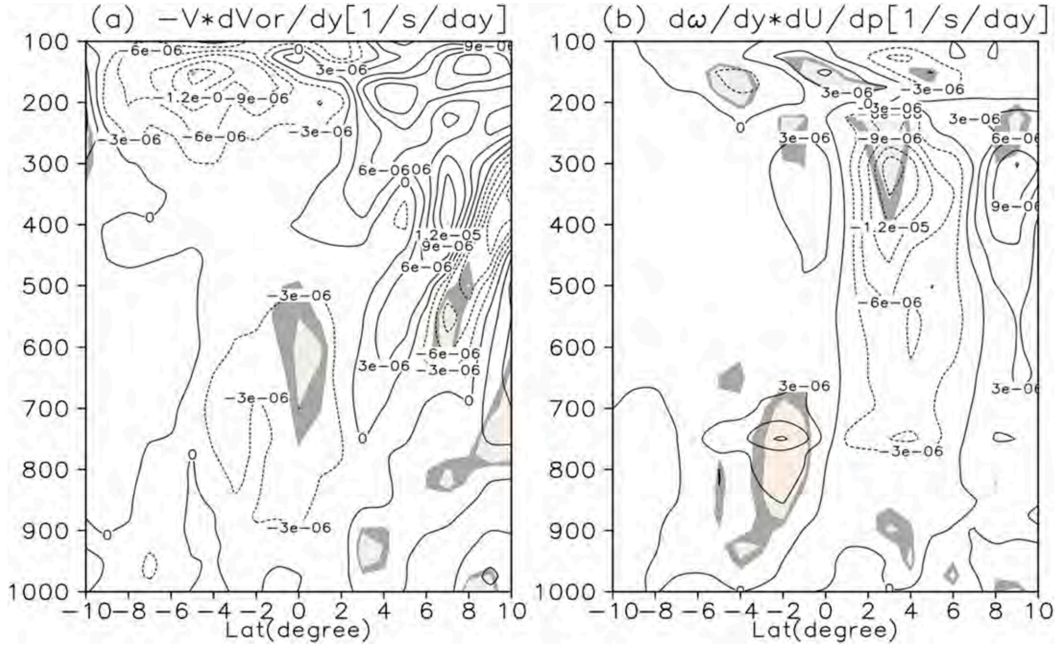

FIG. 4. As in Fig. 3, but for (a) vorticity advection by mean flow and (b) vorticity tendency associated with vertical wind shear and meridional gradients of vertical velocity.

4. Mechanisms of the meridional propagations of the HF-ISOs

Regarding the PR1606, the southward propagation of the HF-ISO occurs over the landmass, and the northward one exists not only over the landmass but also over the SCS (Fig. 2). For the convenience of analysis and comparison, the northward propagation of the HF-ISO is divided into two parts including over the SCS before 9 June and over the landmass after 10 June.

a. Mechanisms of the southward propagation

Figure 3 shows the meridional–vertical structure of the composite southward-propagating HF-ISO from JRA-55. It is indicated that maximum vertical motion occurs at 400–300 hPa and coincides with the convection center (Fig. 3a). Associated with this maximum ascending motion are the low-level convergence and the upper-tropospheric divergence (Fig. 3d). It is worth noting that the convergence in the planetary boundary layer (PBL) tends to lead the convection by around 2°, and the PBL maximum specific humidity, air temperature, and the minimum geopotential height also shift to the south of the convection center, thus implying that they could drive the HF-ISO southward. Meanwhile, a significant baroclinic structure appears in vorticity field near the convection center (Fig. 3b), though the vertical wind shear results in a positive vorticity with an equivalent barotropic structure to the south of the maximum precipitation anomalies (Fig. 4b) and the vorticity advection leads a similar structure but with opposite sign (Fig. 4a). For the first half of June, the background vertical wind shear is very weak over south China and the mean meridional wind is southerly (Figs. 5a and 5b), which has a negative contribution to the southward propagation. That implies the tendency of positive barotropic vorticity, including the vertical wind shear effect (Jiang et al. 2004; Drbohlav and Wang 2005; M. Wang et al. 2017) and the vorticity advection effect (Bellon and Sobel 2008), is not a key cause for the southward propagation of the HF-ISO.

Figure 6 shows the same composite by the NCEP–NCAR reanalysis. By comparison, one can find that most of the features from the JRA-55 reanalysis. For instance, the southward shifts of the low-level specific humidity, air temperature, and geopotential height and the baroclinic structure of the vorticity are well reflected by the NCEP–NCAR reanalysis. So hereafter we analyzed the meridional–vertical structure of the HF-ISOs just by the JRA-55 reanalysis unless specifically pointed out.

From Fig. 7a, one can see that maximum sea surface/land skin temperature (SST/LST) is a few degrees to the south of the convection center, while a minimum appears to the north of the convection center. Warm sea surface/land skin temperature anomalies usually induce positive sensible heat flux anomalies, which can destabilize the atmosphere and induce low-level convergence and favor the ISOs moving northward (Webster 1983;

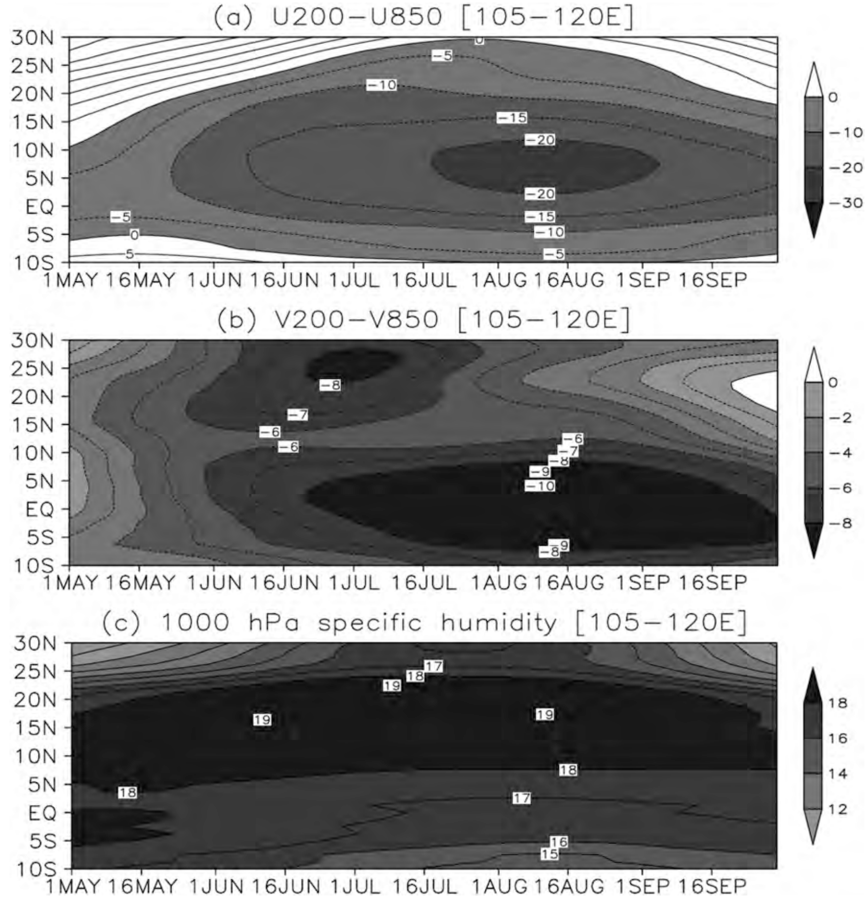

FIG. 5. Summer mean state of (a) vertical wind shear (200–850-hPa zonal winds; m s^{-1}), (b) differences of meridional winds between 200 and 850 hPa (200–850 hPa; m s^{-1}), and (c) 1000-hPa specific humidity (g kg^{-1}).

Kemball-Cook and Wang 2001). It is worth noting that the SST/LST tendency (Fig. 7b) appears to be a maximum value to the south of the maximum SST/LST, which implies a maximum SST/LST will appear farther south on the next day and the convection center will move southward. Nevertheless, the sensible heat flux (Fig. 8c) is very different from the distribution of the SST/LST. It implies that the SSH is not an essential mechanism for the southward propagation in this case. Even so, warm SST/LST anomalies can transfer the energy to the atmosphere by longwave radiative flux (Fig. 8d). The SST/LST tendency can be attributed to the shortwave radiation (Fig. 8a), and the latent heat flux anomalies, induced by the meridional wind speed anomalies (Fig. 8f), form an opposite SST/LST tendency. This indicates that the cloud–radiation effect, rather than the wind–evaporation effect, has a contribution to the southward propagation of the HF-ISO.

Besides air–sea/land interaction, low-level moisture convergence induced by horizontal winds is a possible mechanism to drive the HF-ISO southward. Figure 8e shows a positive moisture advection south of the maximum precipitation anomalies. However, these anomalies are dominated by anomalous flow and mean water vapor, not mean flow and anomalous water vapor. This positive moisture advection can be easily understood. To the north of 20°N, the background moisture decreases from the coastal region to inland (Fig. 5c), and so the meridional gradient of the mean specific humidity is negative. In response to the HF-ISO convective heating, the perturbation wind has a southward flow to the north and a northward flow to the south of the convection center (Fig. 8f). As a result, the moist perturbation has an asymmetric structure with a positive center appearing to the south of the convection center and a negative center to the north of the convection (Fig. 8e). By contrast, the moisture advection by the mean flow is very small, because the background of southerly winds is the same order as the anomalous winds and the mean water vapor is an order

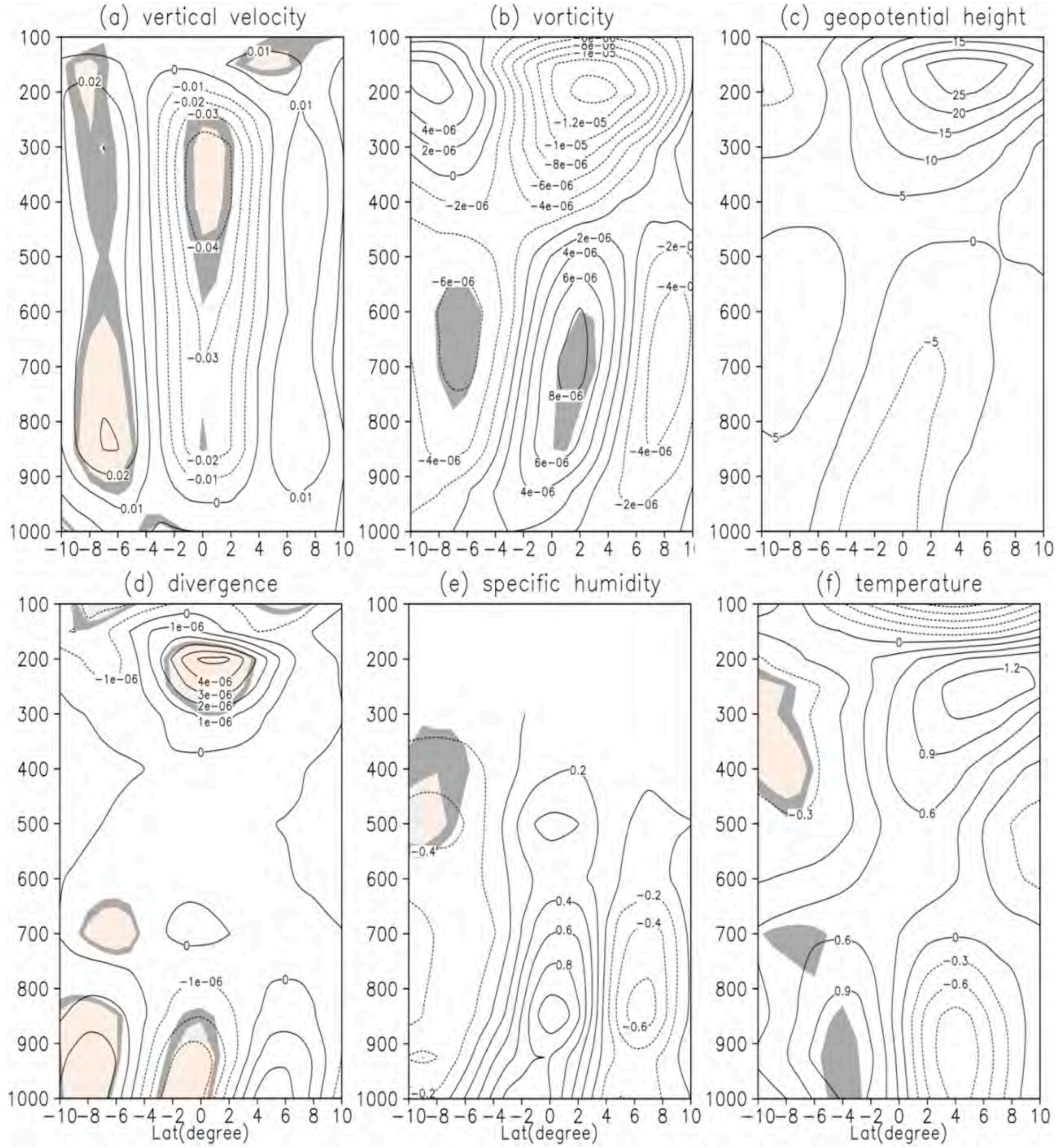

FIG. 6. As in Fig. 3, but for NCEP–NCAR reanalysis.

of magnitude larger than the anomalies. We note that maximum moisture anomalies are located at about 800 hPa, so the moisture advection and water vapor are integrated from 1000 to 700 hPa with a mass weight as Fig. 9. From Fig. 9b, the low-level moisture appears to be an asymmetric distribution as showed in Fig. 3e. This could favor southward-propagating ISOs. Meanwhile, the low-level moisture advection by the mean flow would weaken the contribution of the moisture advection effect to the southward-propagating HF-ISO.

Figure 10 shows relationships between HF-ISO convection and other variables more clearly. From Fig. 10a, one can see that the downward solar radiation anomalies lead the surface air temperature anomalies that then

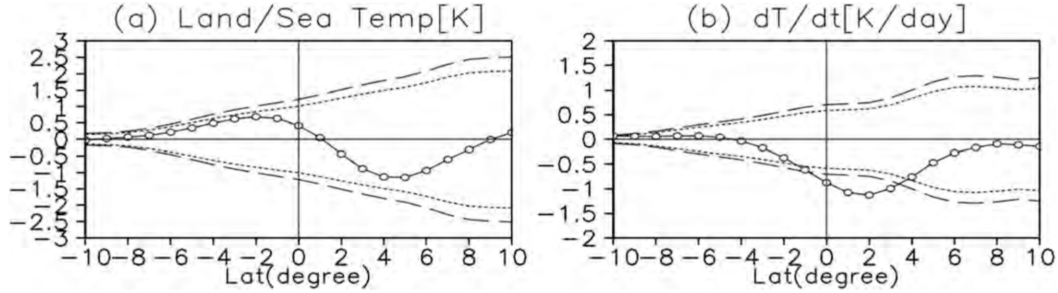

FIG. 7. As in Fig. 3, but for one-dimensional composites of (a) sea surface temperature/land skin temperature (K) and (b) tendency (K day^{-1}) from NCEP–NCAR reanalysis. The dotted line and dashed lines indicate the significance test with 90% and 95% confidence levels, respectively.

induced the low pressure at the surface, and then a convection center appears. The upward latent heat flux anomalies and moisture advection are almost in phase, and they lead the positive surface specific humidity anomalies (Fig. 10b). Last is also convection. Both vorticity and divergence anomalies are almost in phase with the convection (Figs. 10c and 10d), and the lead vorticity tendency induced by advection and vertical wind shear mechanism have an opposite sign as mentioned before.

b. *Mechanisms of the northward propagation over the SCS*

Figure 11 shows the meridional–vertical structure of the composite northward-propagating HF-ISO. From

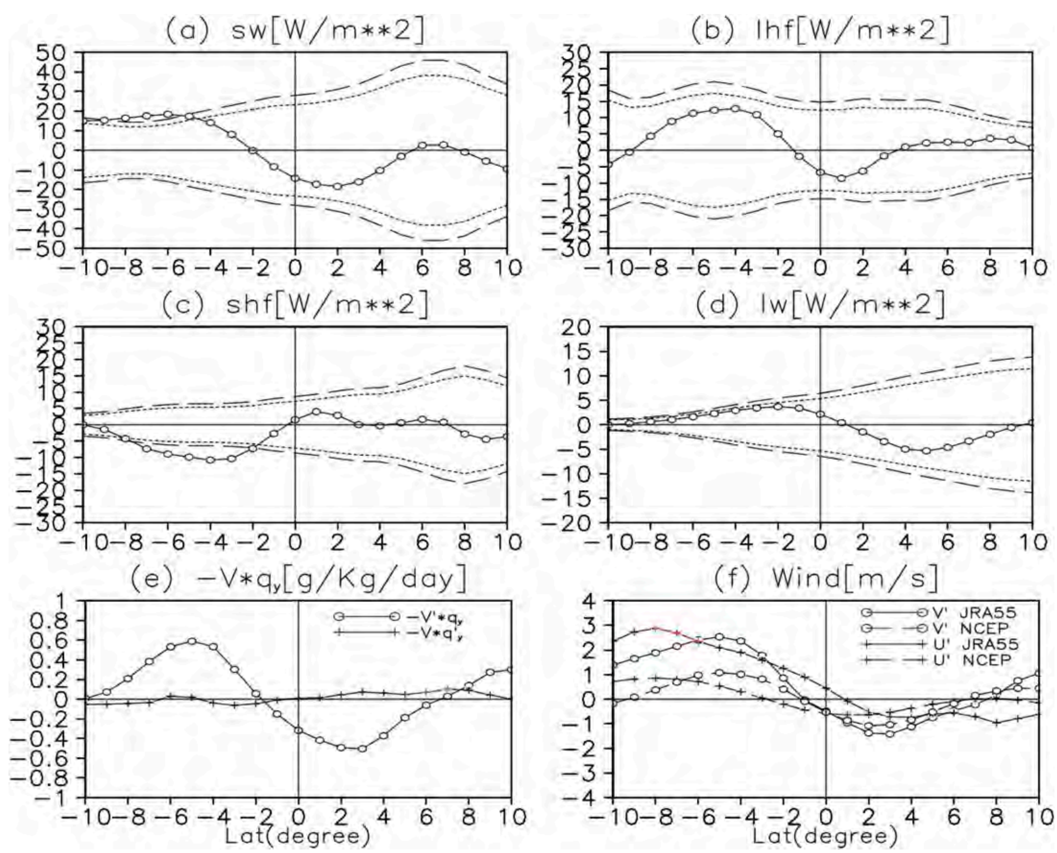

FIG. 8. As in Fig. 7, but for (a) surface solar radiation (W m^{-2}), (b) surface latent heat flux (W m^{-2}), (c) surface sensible heat flux (W m^{-2}), (d) surface upward longwave radiation (W m^{-2}), (e) moisture advection (mm day^{-1}) at 1000 hPa, and (f) wind anomaly (m s^{-1}) at 1000 hPa from NCEP–NCAR reanalysis. The positive latent heat flux, sensible heat flux and longwave radiation mean upward fluxes, and the positive solar radiation mean downward flux. The red and green marks denote the composite anomalies exceeding 90% and 95% confidence levels, respectively.

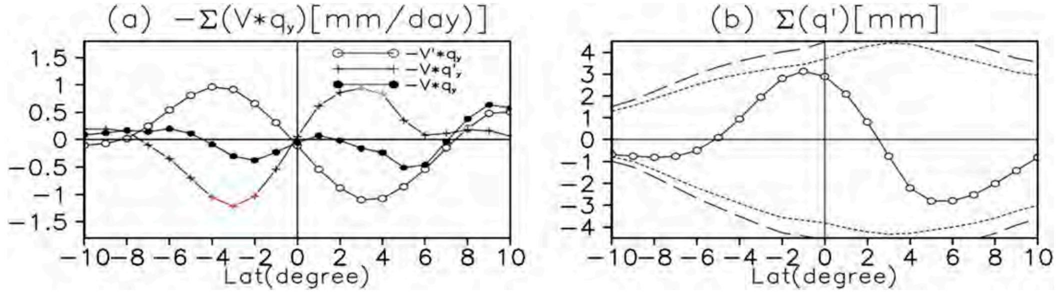

FIG. 9. As in Fig. 8, but for (a) integration of moisture advection and (b) integrated moisture from 1000 to 700 hPa with a mass weight; $-\mathbf{V} \cdot q_y$, a sum of $-\mathbf{V}' \cdot q_y$ and $-\mathbf{V} \cdot q'_y$, denotes moisture advection effect.

Fig. 11a, one can see that maximum vertical motion still occurs over the convection center. Obviously, the low-level ascending flows shift northward and there are other variations as well. A distinctive feature, compared to the southward-propagating HF-ISO, is a positive vorticity center with an equivalent barotropic structure located north of the convection center. The barotropic vorticity can be induced by both the vertical wind shear effect (Jiang et al. 2004; Drbohlav and Wang 2005; M. Wang et al. 2017) and the vorticity advection effect (Bellon and Sobel 2008), although contribution associated with the latter is larger than that related to the former (as shown in Fig. 12). It implies that the tendency of positive barotropic vorticity plays a key role in the northward propagation of the HF-ISO over the SCS. Moreover, the vorticity advection effect is more important than the vertical wind shear effect in this case.

Figure 13a shows SST/LST anomalies relative to the position of the precipitation maximum. Warm SST/LST anomalies are found more than 5° north of the convection center. Compared to those in the southward-propagation case, they are much weaker and farther

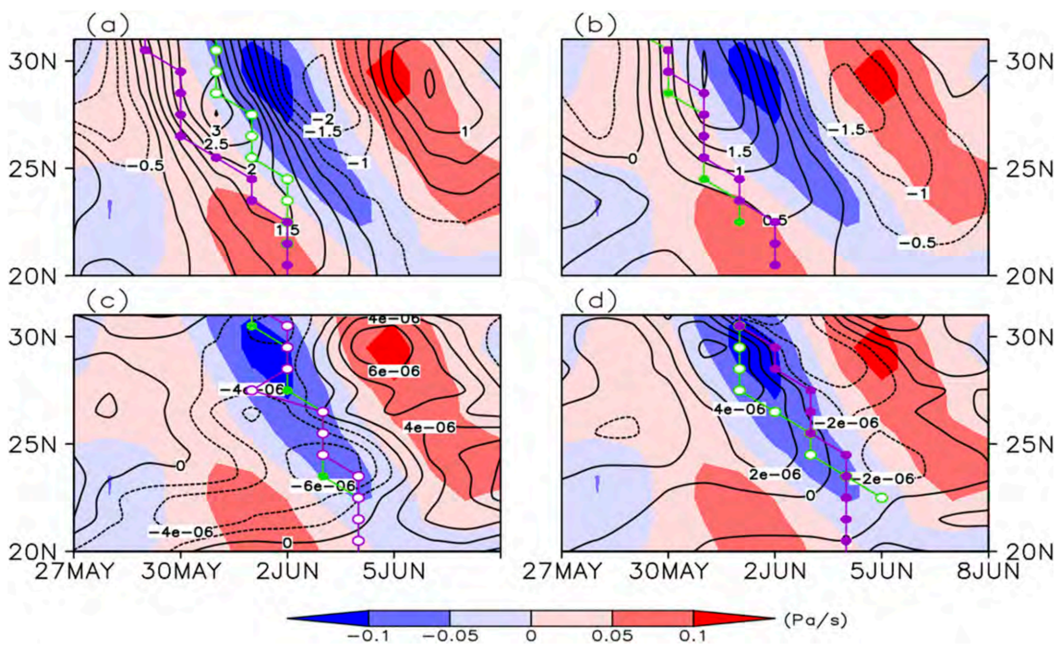

FIG. 10. Hovmöller diagrams of 5–20-day-filtered variables with 400-hPa vertical velocity (Pa s^{-1}) shaded. (a) Surface air temperature (contour, K), maximum surface solar radiation (downward flux, purple line, W m^{-2}), and minimum surface geopotential height (green line, gpm); (b) specific humidity (contour, g kg^{-1}), maximum moisture advection by anomalous flow (green line, kg day^{-1}), and maximum latent heat flux (upward flux, purple line, W m^{-2}); (c) barotropic vorticity tendency induced by advection (contour, s^{-1} day^{-1}), maximum vorticity at 850 hPa (green line, s^{-1}), and minimum vorticity at 200 hPa (purple line); and (d) barotropic vorticity tendency induced by the vertical wind shear effect (contour, s^{-1} day^{-1}), maximum divergence at 200 hPa (green line, s^{-1}), and minimum divergence at 200 hPa (purple line).

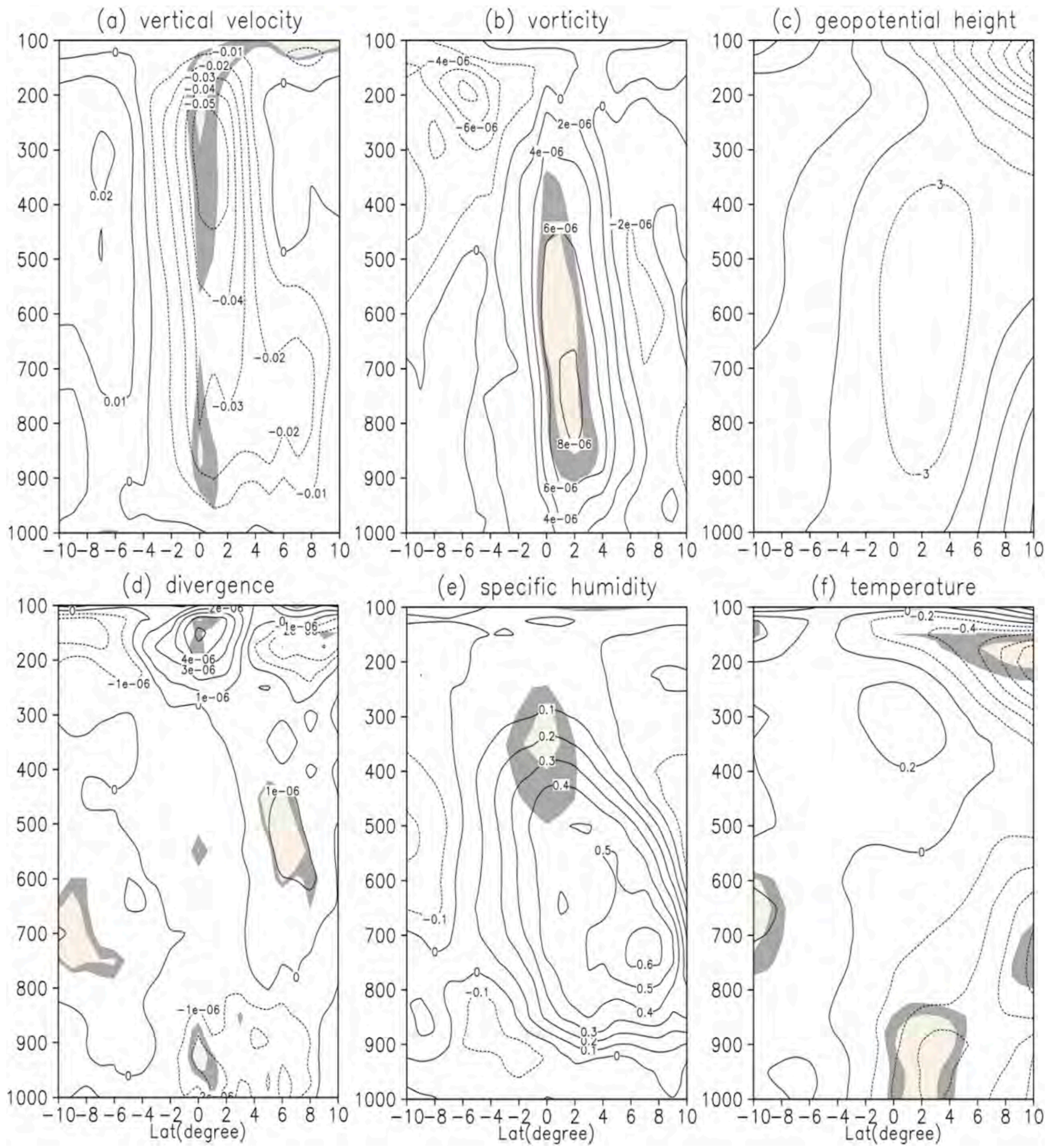

FIG. 11. As in Fig. 3, but for composites of the northward-propagating HF-ISO over the South China Sea.

away from the precipitation maximum. In response to the warm SST/LST anomalies, a positive SSH and longwave radiation appear farther north of the convection (Figs. 14c and 14d). Thus, the SST/LST anomalies or SSH should not be a dominant factor here, but it does create a favorable condition for ISOs propagating northward. In this case, the surface solar radiation anomalies, resulted from the HF-ISO precipitation, have different distribution from the SST/LST anomalies and their tendency. Examining the distributions of both surface fluxes, the latent heat flux is clearly more similar to the SST/LST tendency than the surface solar radiation. This might imply that latent heat flux is more dominant in affecting SST than solar radiation over the SCS in this case. We

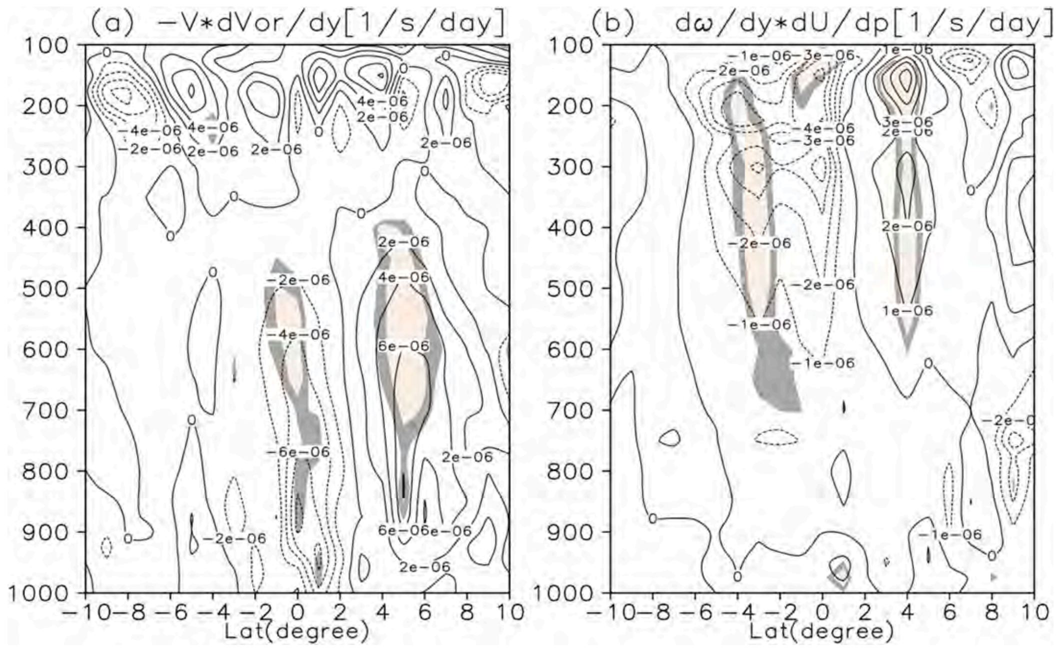

FIG. 12. As in Fig. 4, but for composites of the northward-propagating HF-ISO over the South China Sea.

note that the latent heat flux changes have similar pattern to those changes in surface wind speed shown in Fig. 14f. In other words, the latent heat flux and SST/LST tendency over this region are mainly controlled by surface winds.

In addition, a positive moisture center appears north of the convection center at the 800–700-hPa level (Fig. 11e), which would favor the HF-ISO moving northward. For surface moisture advection, there is an opposite sign between the two terms shown in Fig. 14e. Although the moisture center is located at a low-level atmosphere, large magnitudes also appear in mid- and high-level moisture (Fig. 11e). So we need consider column-integrated water vapor from 1000 to 100 hPa as shown in Fig. 15. From Fig. 15b, one can see that maximum column-integrated moisture is about 3°N of the convection center. Also, a positive column-integrated moisture tendency is found north of the precipitation maximum, which will lead to the northward displacement of the convective heating and thus the convection tends to move northward.

In summary, both the vertical wind shear effect and the vorticity advection effect are important mechanisms of the northward propagation of the HF-ISO over the SCS in this case. By comparison, the latter provides a larger contribution than the former that is also found in Figs. 16c and 16d. Air–sea/land interaction mainly via wind–evaporation–SST/LST feedback process will lead to a warm SST/LST north of the convection center. Thus, more SSH and longwave radiation should destabilize the atmosphere and induce a favorable condition for ISOs propagating northward though they appear much farther north of the convection center. In particular, Fig. 16a shows an out-of-phase relationship between the convection and surface air temperature anomalies. Furthermore, the maximum surface moisture advection appears north of the convection center (Figs. 14e and 15b).

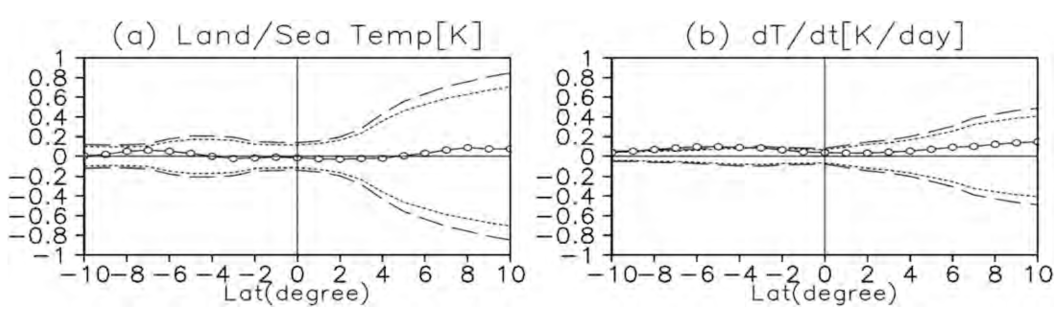

FIG. 13. As in Fig. 7, but for composites of the northward-propagating HF-ISO over the South China Sea.

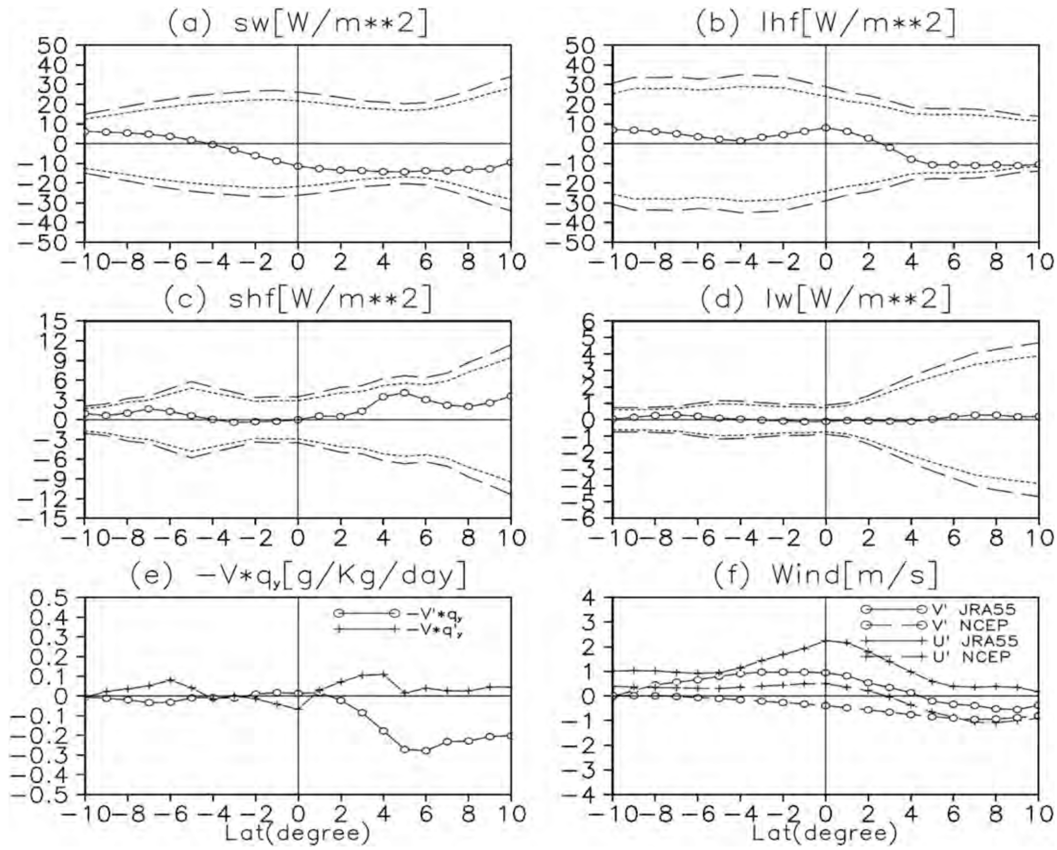

FIG. 14. As in Fig. 8, but for composites of the northward-propagating HF-ISO over the South China Sea.

We take column integration into account because the large moisture anomalies are distributed in almost all of levels. The results show that the wet advection is located north of the convection center, which will favor the HF-ISO moving northward.

c. *Mechanisms of the northward propagation over southern China*

The meridional–vertical structure of the composite northward-propagating HF-ISO over southern China (Fig. 17) is similar to that over the SCS (Fig. 11). However, the low-level convergence is found in two centers on both sides of the convection center in Fig. 17d. By comparison, only one center is located north of the convection center though the low-level convergence is also found on both sides in the NCEP–NCAR reanalysis (not shown). The vorticity tendency associated with vertical wind shear appears to be an unclear barotropic structure (Fig. 18b). Thus, the northward shift of positive barotropic vorticity (Fig. 17b) cannot be explained by the vertical wind shear effect. In another way, from Fig. 18a, we can see that the positive vorticity tendency with an

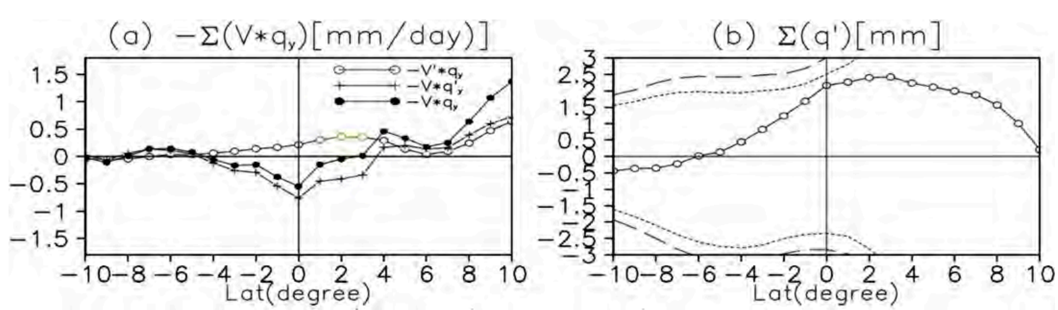

FIG. 15. As in Fig. 9, but for integration from 1000 to 100 hPa with a mass weight.

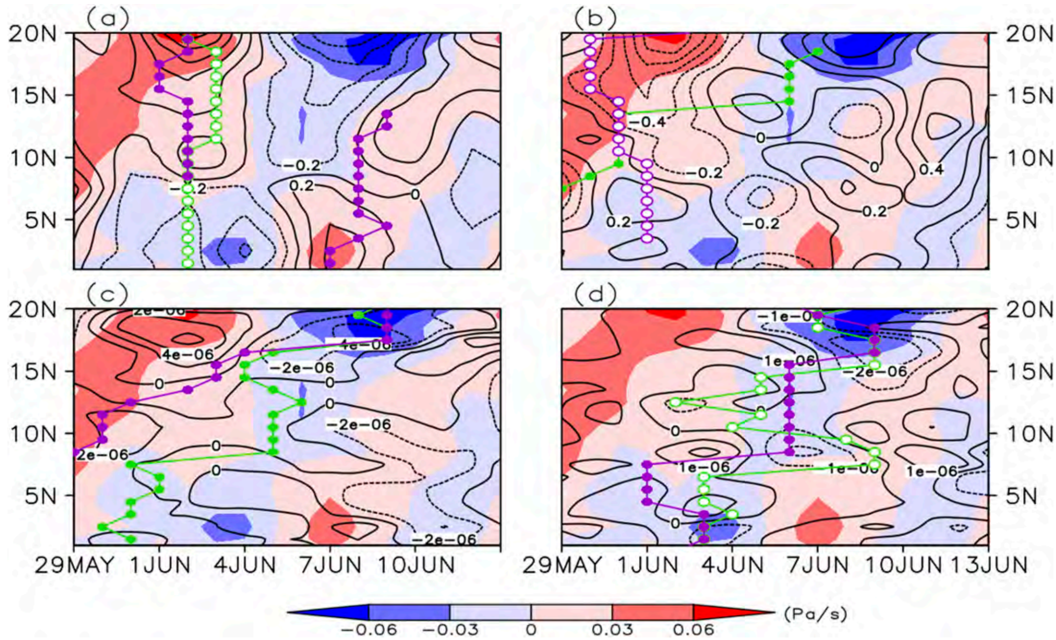

FIG. 16. As in Fig. 10, but for the northward-propagating HF-ISO over the South China Sea.

equivalent barotropic structure induced by mean flow appear north of the maximum precipitation anomalies. It implies that the vorticity advection effect is still an important mechanism for the northward-propagating HF-ISO over southern China.

Figure 19a shows that the positive SST/LST anomalies lie on both sides of the convection center and Fig. 20d illustrates the similar distribution of the longwave radiation. From Figs. 20a and 20b, one can see that the surface shortwave radiation and latent heat flux reversely contribute to the SST/LST tendency, and the latter is induced by the anomalous surface winds (Fig. 20f). The resulted SST/LST tendency shown in Fig. 19b implies a cooling over almost the entire domain. Overall, the SST/LST anomalies are not a key factor for the northward propagation of the HF-ISO over southern China in this case, though the positive SSH anomalies are found north of the convection (Fig. 20c) that favor the HF-ISO moving northward to some extent.

Figure 20e shows a positive surface moisture advection south of the maximum precipitation anomalies. The other distinct feature is shown in the specific humidity field with a maximum moisture center located at about 500 hPa (Fig. 17e), which is much higher than the first two cases. We calculated column-integrated water vapor from 1000 to 100 hPa as shown in Fig. 21. From Fig. 21b, one can see that maximum column-integrated moisture is about 1°N of the convection center. Also, a positive column-integrated moisture tendency by mean flow and anomalous water vapor is found north of the precipitation maximum that will lead to the northward displacement of the convective heating and thus favor the convection moving northward. In contrast, negative moisture tendency by anomalous flow and mean water vapor will weaken the contribution of the moisture advection effect. Overall, the horizontal moisture advection should not induce the northward-propagating HF-ISOs over southern China. Instead, it would suppress the HF-ISO.

The abovementioned is also illustrated in Fig. 22. The relationships between the convection and surface air temperature, moisture advection, and vorticity tendency induced by vertical wind shear are not close (Fig. 22a, 22b, and 22d). Figure 22c shows that the barotropic vorticity tendency induced by advection leads the convection, which favors the HF-ISO moving northward.

5. Summary and discussion

PRs, influenced by both the tropical and subtropical monsoons, often occur in south China and cause severe property damages (Zheng et al. 2007). The PR1606 event is also connected closely to the effects from the tropics and midlatitudes that are manifested by meridional propagation of the ISO with a 5–20-day period (viz., HF-ISO). In the PR1606, dominant mechanisms are different between the southward and northward propagation of the HF-ISOs. Even in the cases of northward propagation, there is a different influence of each mechanism between the SCS and southern China. The major findings made in this study are summarized and discussed as follows:

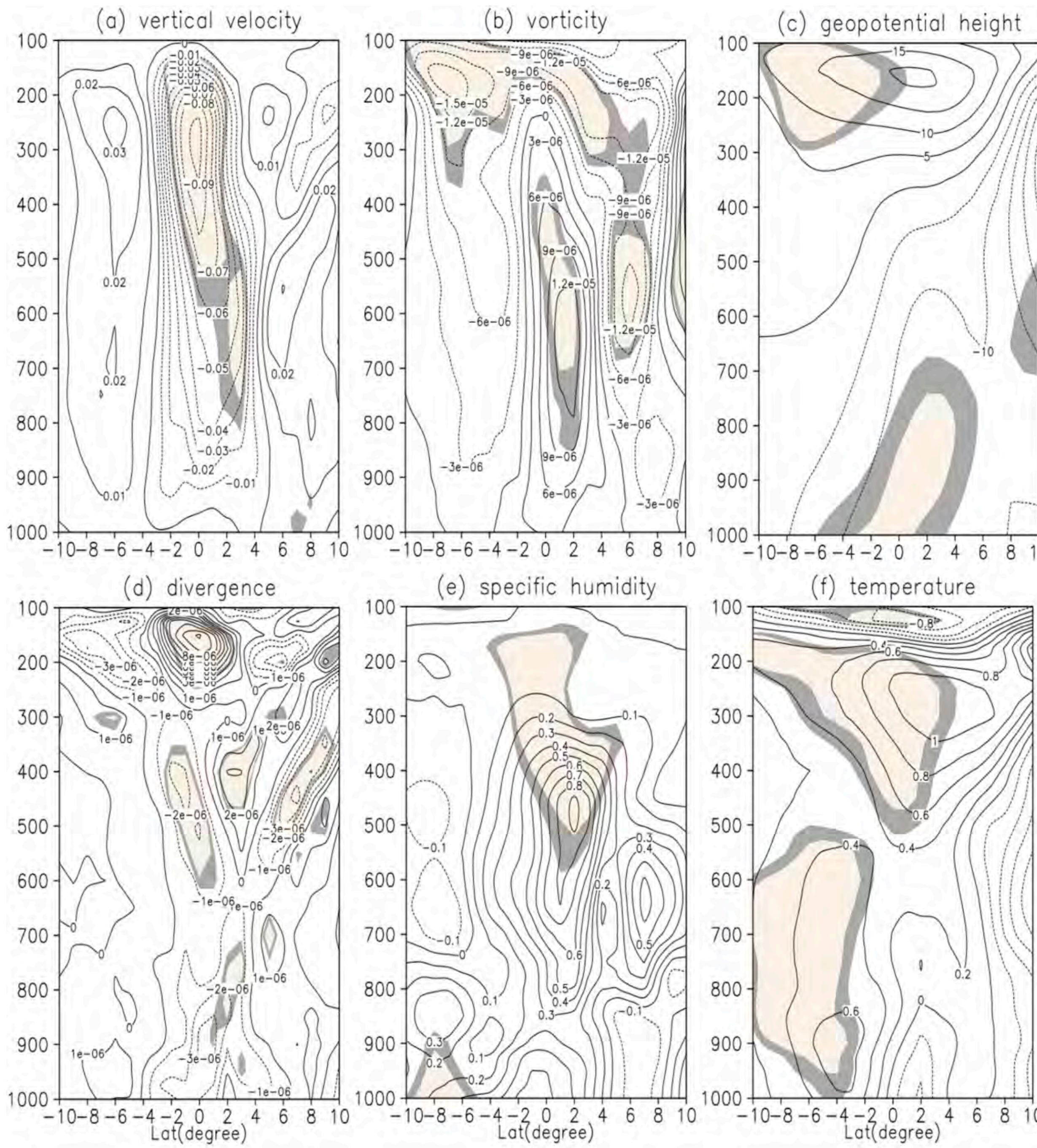

FIG. 17. As in Fig. 3, but for composites of the northward-propagating HF-ISO over southern China.

1) Over southern China, the internal atmospheric dynamics, including the vertical wind shear effect (Jiang et al. 2004; Drbohlav and Wang 2005; M. Wang et al. 2017) and the vorticity advection effect (Bellon and Sobel 2008), are not essential to cause the southward propagation of the HF-ISO in the PR1606. Moisture advection plays an important role in the southward shift of the convective zone. These anomalies are dominated by anomalous flow and mean water vapor, not mean flow and anomalous water vapor. The cloud–radiation effect may be, at least partially, responsible for the southward propagation. First, the convection center with larger precipitation anomalies reduces surface solar radiation, and to the south

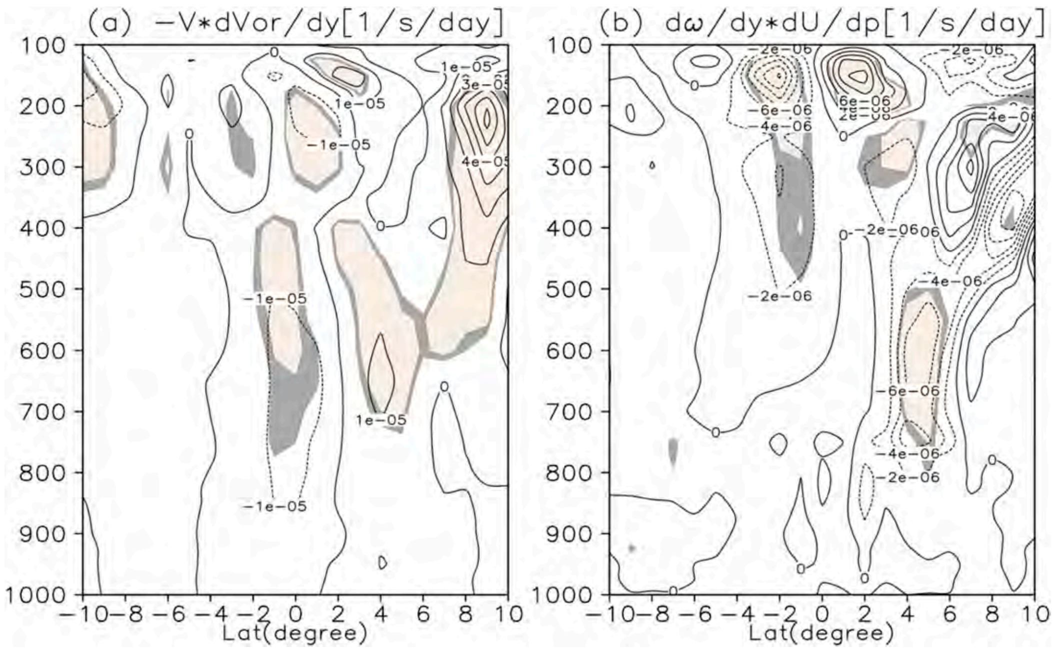

FIG. 18. As in Fig. 4, but for composites of the northward-propagating HF-ISO over southern China.

increases the shortwave radiation because of less cloudiness. Although considerably smaller than the other heating components, warmer SST/LST can transfer the energy to the atmosphere via longwave radiative flux, not SSH flux. And then the destabilized atmosphere induces a low-level convergence ahead of the convection center to favor the HF-ISO moving southward.

2) Over the SCS, the northward propagation of the HF-ISO is mainly attributed to the vertical wind shear effect and the vorticity advection effect, and the latter is relatively more important than the former in this case. Moisture advection is a supplementary effect caused by inducing a weak positive moisture tendency north of the convection center. Different from the case of southward propagation, the anomalous water vapor advected by mean flow is dominant as well as the mean water vapor advected by the anomalous flow. Furthermore, the SST/LST anomalies induced by the wind–evaporation effect destabilize the low-level atmosphere north of the convection center via both the SSH and longwave radiation. Nevertheless, compared to those in the southward-propagation case, they are much weaker and farther away from the precipitation maximum. Thus, the SST/LST anomalies or SSH should not be a dominant factor here.

3) Two possible mechanisms are proposed to explain the cause of the northward propagation of the HF-ISO over southern China during the PR1606 period. The first is the vorticity advection that is a dominant factor. The second mechanism is the SSH effect that plays a minor role. In this case, the moisture advection is not a key factor contributing to the northward shift of the moisture and the convective heating.

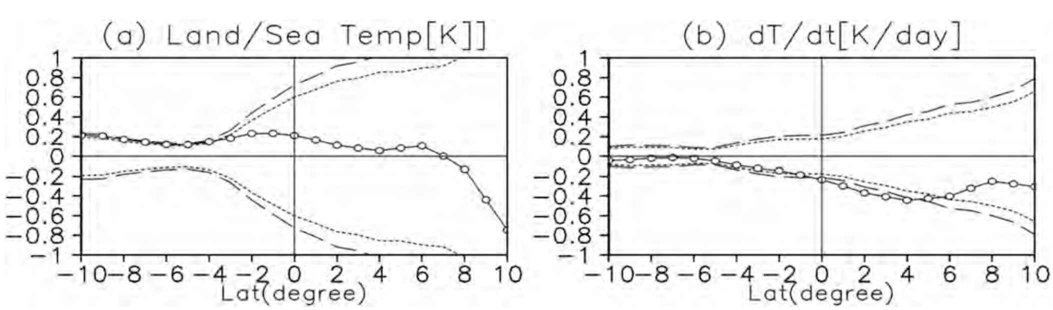

FIG. 19. As in Fig. 7, but for composites of the northward-propagating HF-ISO over southern China.

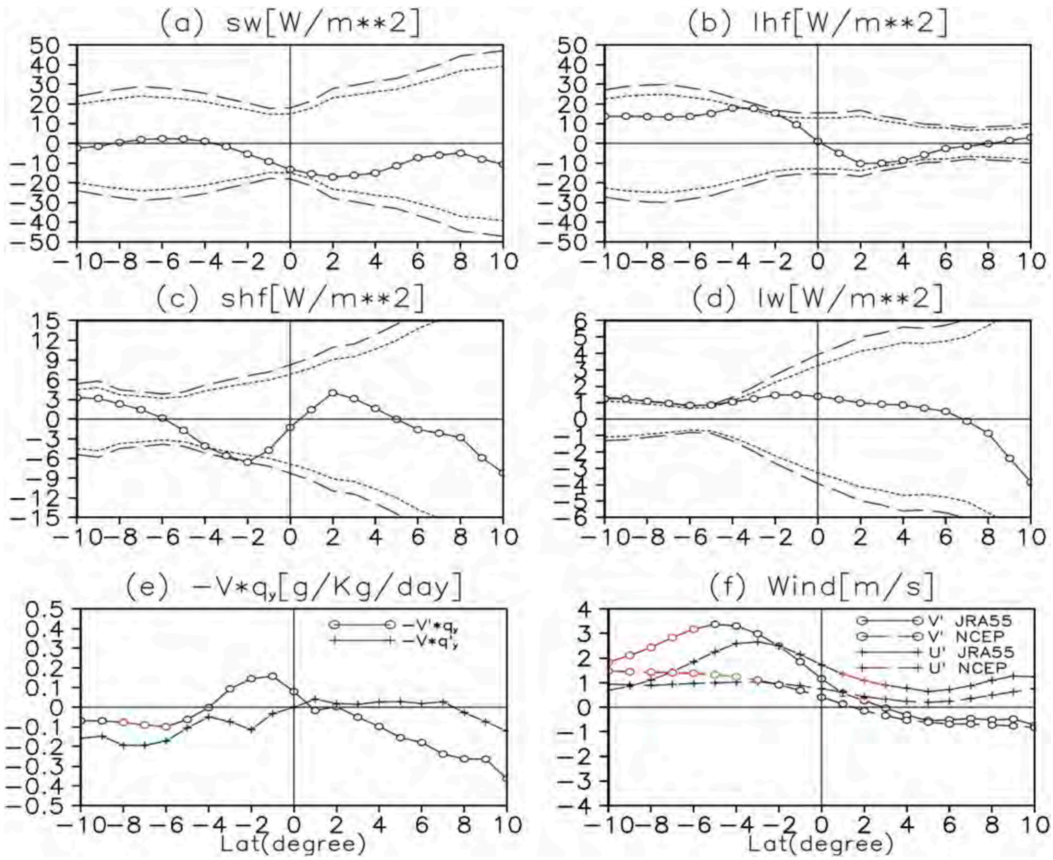

FIG. 20. As in Fig. 8, but for composites of the northward-propagating HF-ISO over southern China.

Some differences are shown between the southward and northward propagation of the HF-ISO over southern China in this case. The positive specific humidity anomalies concentrate in the lower troposphere in the southward-propagating case and at the midtroposphere in the northward-propagating one over southern China. This results from the different vertical gradients of the background moisture. In mid-June, mean water vapor invades more northward so that the vertical gradients of the moisture around the convection center are larger than those in early June. Thus, there are positive specific humidity anomalies in the midtroposphere because the enlarged vertical gradients of the moisture and the large vertical velocity mainly exist in the mid- to upper troposphere. Moreover, there are different mechanisms between the southward and northward propagation of the HF-ISO over southern China. As mentioned above, the moisture advection by the anomalous flow and mean water vapor and the cloud–radiation effect are key factors for the southward-propagating HF-ISO, while the

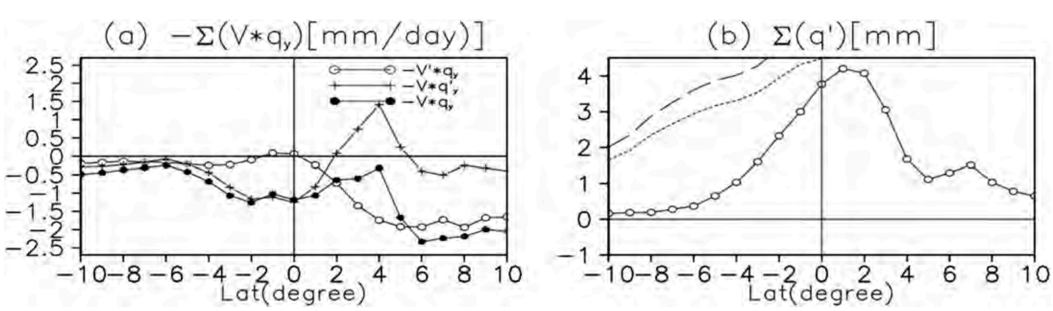

FIG. 21. As in Fig. 9, but for composites of the northward-propagating HF-ISO over southern China.

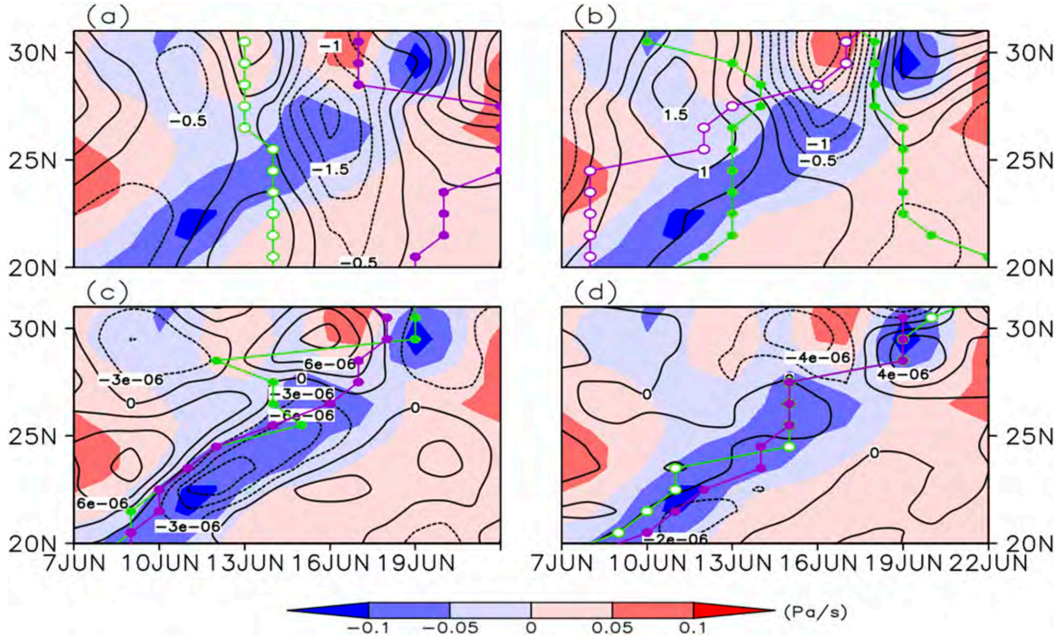

FIG. 22. As in Fig. 10, but for the northward-propagating HF-ISO over southern China.

vorticity advection and the wind–evaporation effect contribute to the northward propagation of the HF-ISO over southern China.

Differences between the meridional propagation of the HF-ISOs over southern China and over the SCS are mainly attributed to the mean state of circulation and moisture. As shown in Fig. 5a, the vertical wind shears in June almost have an opposite sign relative to the coast junction. So the vertical wind shear effect works in the northward propagation of the HF-ISOs over the

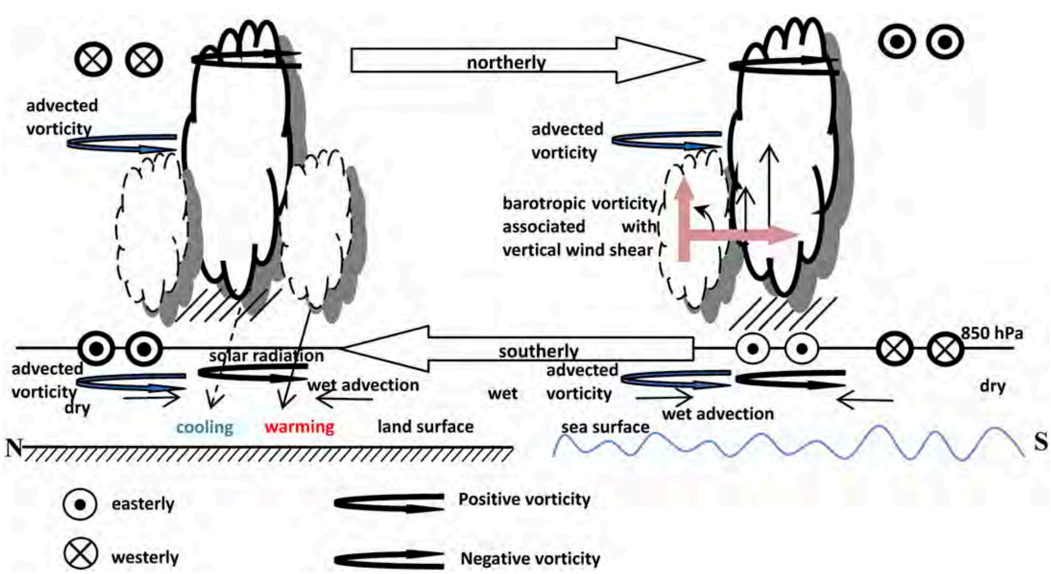

FIG. 23. Schematic diagram for mechanisms of meridional-propagating HF-ISO associated with PR1606. Background in June (105°–120°E): easterly vertical shear over the SCS, positive meridional gradients of mean surface moisture over the SCS and negative over southern China, and negative differences of meridional winds between 200 and 850 hPa over the SCS and southern China. Main mechanisms: (for northward-propagating HF-ISO over the SCS) vorticity advection effect by the basic-state baroclinic meridional wind, barotropic vorticity associated with vertical wind shear and moisture advection effect; (for northward-propagating HF-ISO over southern China) vorticity advection effect; and (for southward-propagating HF-ISO over southern China) cloud–radiation effect and moisture advection effect by anomalous flow and mean water vapor.

SCS, but not in both the southward and northward one over southern China. While the difference of meridional winds between 200 and 850 hPa is less than zero over southern China and SCS in throughout summer (Fig. 5b), the vorticity advection mechanism dominates the northward propagation of the HF-ISOs over both the SCS and southern China, and suppresses the southward one. For mean surface moisture, there are negative meridional gradients over southern China and positive ones over the SCS (Fig. 5c). Thus, positive moisture advection by anomalous flow appears north of the convection over the SCS that favors HF-ISOs moving northward, and to the south of the convection over southern China that drives HF-ISO moving southward. For the northward propagation of the HF-ISOs over southern China, moisture advection by anomalous flow has a negative contribution. Figure 23 shows the main mechanisms of meridional-propagating HF-ISOs associated with the PR1606.

Previous studies have shown that PBL horizontal moisture advection plays an important role in northward propagation of the ISOs (Jiang et al. 2004). Although the moisture tendency induced by the mean flow and the anomalous water vapor is a key factor for the northward-propagating LF-ISOs over the Indian Ocean, the horizontal moisture advection suppresses the LF-ISO over the western North Pacific (Chou and Hsueh2010). For northward-propagating HF-ISO with a 10–20-day period, M. Wang et al. (2017) regard the moisture advection by mean flow as one of main mechanisms to the north of 20°N. In this study, the horizontal moisture advection should not induce the northward-propagating HF-ISOs over southern China. The result needs an examination in statistics since this study is on the basis of the PR1606 event.

In this study, the SSH is one of the factors driving the HF-ISO northward over southern China, which would be consistent with some previous studies (Webster 1983; Wang et al. 2006; Klingaman et al. 2008; M. Wang et al. 2017). To some extent, the wind–evaporation effect, not the cloud–radiation effect, is responsible for the northward propagation of the HF-ISO over the SCS in the PR1606 event. This is different from the results found in Cao et al. (2017). They conclude that the cloud–radiation effect is a dominant factor, with a supplementary effect from the wind–evaporation effect, for the SST propagation on a 10–20-day time scale in the SCS–WNP region. This study is concerned with the intraseasonal convection propagation in the PR1606, while Cao et al. (2017) focused on the intraseasonal-propagating SST based on a large amount of cases. That is a possible reason for the difference between them.

Acknowledgments. This work is supported by the Science and Technology Program of Guangzhou (Grant 201607010153), Science and Technology Program of Guangdong Province (Grant 2017B030314140), and National Natural Science Foundation of China (Grants 41705089, 41675096, 41505067, and 41575043). The JRA-55reanalysis data were obtained from ftp://ds.data.jma.go.jp. The NCEP–NCAR reanalysis data and OISST.v2 data were obtained from ftp://ftp.cdc.noaa.gov/. The GPI data were obtained from http://ftp.cpc.ncep.noaa.gov/precip/gpi.

REFERENCES

Bellon, G., and A. H. Sobel, 2008: Instability of the axisymmetric monsoon flow and intraseasonal oscillation. *J. Geophys. Res.*, **113**, D07108, https://doi.org/10.1029/2007JD009291.

Boos, W. R., and Z. Kuang, 2010: Mechanisms of poleward propagating, intraseasonal convective anomalies in cloud system-resolving models. *J. Atmos. Sci.*, **67**, 3673–3691, https://doi.org/10.1175/2010JAS3515.1.

Cao, X., R. Wu, and S. Chen, 2017: Contrast of 10–20-day and 30–60-day intraseasonal SST propagation during summer and winter over the South China Sea and western North Pacific. *Climate Dyn.*, **48**, 1233–1248, https://doi.org/10.1007/s00382-016-3138-z.

Chen, J., Z. Wen, R. Wu, Z. Chen, and P. Zhao, 2015: Influences of northward propagating 25–90-day and quasi-biweekly oscillations on eastern China summer rainfall. *Climate Dyn.*, **45**, 105–124, https://doi.org/10.1007/s00382-014-2334-y.

Chou, C., and Y.-C. Hsueh, 2010: Mechanisms of northward-propagating intraseasonal oscillation—A comparison between the Indian Ocean and the western North Pacific. *J. Climate*, **23**, 6624–6640, https://doi.org/10.1175/2010JCLI3596.1.

DeMott, C. A., C. Stan, and D. A. Randall, 2013: Northward propagation mechanisms of the boreal summer intraseasonal oscillation in the ERA-Interim and SP-CCSM. *J. Climate*, **26**, 1973–1992, https://doi.org/10.1175/JCLI-D-12-00191.1.

Drbohlav, H.-K. L., and B. Wang, 2005: Mechanism of the northward-propagating intraseasonal oscillation: Insights from a zonally symmetric model. *J. Climate*, **18**, 952–972, https://doi.org/10.1175/JCLI3306.1.

Fu, S., H. Wang, J. Sun, and Y. Zhang, 2016: Energy budgets on the interactions between the mean and eddy flows during a persistent heavy rainfall event over the Yangtze River valley in summer 2010. *J. Meteor. Res.*, **30**, 513–527, https://doi.org/10.1007/s13351-016-5121-3.

Gao, J., H. Lin, L. You, and S. Chen, 2016: Monitoring early-flood season intraseasonal oscillations and persistent heavy rainfall in South China. *Climate Dyn.*, **47**, 3845–3861, https://doi.org/10.1007/s00382-016-3045-3.

Goswami, B. N., and J. Shukla, 1984: Quasi-periodic oscillations in a symmetric general circulation model. *J. Atmos. Sci.*, **41**, 20–37, https://doi.org/10.1175/1520-0469(1984)041<0020:QPOIAS>2.0.CO;2.

——, and P. K. Xavier, 2003: Potential predictability and extended range prediction of Indian summer monsoon breaks. *Geophys. Res. Lett.*, **30**, 1966, https://doi.org/10.1029/2003GL017810.

Gu, D., and W. Zhang, 2012: The strong dragon-boat race precipitation of Guangdong in 2008 and quasi-10-day oscillation. *J. Trop. Meteor.*, **18** (3), 347–359.

——, Z. Ji, A. Lin, C. Li, and B. Zheng, 2013: The oscillation of Guangzhou daily precipitation and its simple harmonic wave model for extended-range forecasts (in Chinese). *J. Trop. Meteor.*, **29** (6), 899–906.

Hong, W., and X. Ren, 2013: Persistent heavy rainfall over South China during May–August: Subseasonal anomalies of circulation and sea surface temperature. *Acta Meteor. Sin.*, **27**, 769–787, https://doi.org/10.1007/s13351-013-0607-8.

——, ——, and X. Yang, 2015: The influence of the low-frequency diabatic heating on the low-frequency circulation during the persistent severe rainfall period over South China (in Chinese). *Acta Meteor. Sin.*, **73** (2), 276–290.

Huang, D.-Q., J. Zhu, Y.-C. Zhang, J. Wang, and X.-Y. Kuang, 2015: The impact of the East Asian subtropical jet and polar front jet on the frequency of spring persistent rainfall over Southern China in 1997–2011. *J. Climate*, **28**, 6054–6066, https://doi.org/10.1175/JCLI-D-14-00641.1.

Huffman, G. J., R. F. Adler, M. M. Morrissey, D. T. Bolvin, S. Curtis, R. Joyce, B. McGavock, and J. Susskind, 2001: Global precipitation at one-degree daily resolution from multisatellite observations. *J. Hydrometeor.*, **2**, 36–50, https://doi.org/10.1175/1525-7541(2001)002<0036:GPAODD>2.0.CO;2.

Hui, P., and J. Fang, 2016a: Comparison of the multi-scale features in two persistent heavy rainfall events in the middle and lower reaches of Yangtze River. *J. Meteor. Res.*, **30**, 528–546, https://doi.org/10.1007/s13351-016-6028-8.

——, and ——, 2016b: Impact of multi-scale oscillations at high and low latitudes on two persistent heavy rainfall events in the middle and lower reaches of the Yangtze River. *J. Meteor. Res.*, **30**, 662–677, https://doi.org/10.1007/s13351-016-6082-2.

Imada, Y., S. Kanae, M. Kimoto, M. Watanabe, and M. Ishii, 2015: Predictability of persistent Thailand rainfall during the mature monsoon season in 2011 using statistical downscaling of CGCM seasonal prediction. *Mon. Wea. Rev.*, **143**, 1166–1178, https://doi.org/10.1175/MWR-D-14-00228.1.

Jiang, X., T. Li, and B. Wang, 2004: Structures and mechanisms of the northward propagating boreal summer intraseasonal oscillation. *J. Climate*, **17**, 1022–1039, https://doi.org/10.1175/1520-0442(2004)017<1022:SAMOTN>2.0.CO;2.

Kalnay, E., and Coauthors, 1996: The NCEP/NCAR 40-Year Reanalysis Project. *Bull. Amer. Meteor. Soc.*, **77**, 437–472, https://doi.org/10.1175/1520-0477(1996)077<0437:TNYRP>2.0.CO;2.

Kang, I.-S., D. Kim, and J.-S. Kug, 2010: Mechanism for northward propagation of boreal summer intraseasonal oscillation: Convective momentum transport. *Geophys. Res. Lett.*, **37**, L24804, https://doi.org/10.1029/2010GL045072.

Karmakar, N., A. Chakraborty, and R. S. Nanjundiah, 2017: Space–time evolution of the low- and high-frequency intraseasonal modes of the Indian summer monsoon. *Mon. Wea. Rev.*, **145**, 413–435, https://doi.org/10.1175/MWR-D-16-0075.1.

Kemball-Cook, S., and B. Wang, 2001: Equatorial waves and air–sea interaction in the boreal summer intraseasonal oscillation. *J. Climate*, **14**, 2923–2942, https://doi.org/10.1175/1520-0442(2001)014<2923:EWAASI>2.0.CO;2.

Klingaman, N. P., H. Weller, J. N. Slingo, and P. M. Inness, 2008: The intraseasonal variability of the Indian summer monsoon using TMI sea surface temperature and ECMWF reanalysis. *J. Climate*, **21**, 2519–2539, https://doi.org/10.1175/2007JCLI1850.1.

Kobayashi, S., and Coauthors, 2015: The JRA-55 reanalysis: General specifications and basic characteristics. *J. Meteor. Soc. Japan*, **93**, 5–48, https://doi.org/10.2151/jmsj.2015-001.

Krishnamurthy, V., and J. Shukla, 2007: Intraseasonal and seasonally persisting patterns of Indian monsoon rainfall. *J. Climate*, **20**, 3–20, https://doi.org/10.1175/JCLI3981.1.

Li, C., J. Liang, B. Zheng, A. Lin, and D. Gu, 2007: The period of South China Sea summer monsoon advanced northward with the related circulation change features (in Chinese). *J. Appl. Meteor. Sci.*, **18** (2), 202–210.

——, T. Li, D. Gu, A. Lin, and B. Zheng, 2015: Relationship between summer rainfall anomalies and sub-seasonal oscillations in South China. *Climate Dyn.*, **44**, 423–439, https://doi.org/10.1007/s00382-014-2172-y.

Li, X., Y. Luo, and Z. Guan, 2014: The persistent heavy rainfall over southern China in June 2010: Evolution of synoptic systems and the effects of the Tibetan Plateau heating. *J. Meteor. Res.*, **28**, 540–560, https://doi.org/10.1007/s13351-014-3284-3.

Liao, Q., and S. Tao, 2004: The seasonal march of atmospheric circulation over East Asia in the late summer and its role in the formation of the regional persistent precipitation anomaly. *Chin. J. Atmos. Sci.*, **28** (6), 835–846.

Lin, A., C. Li, B. Zheng, and D. Gu, 2013: Variation characteristics of sustained torrential rain during the pre-flooding season in Guangdong and the associated circulation pattern (in Chinese). *Acta Meteor. Sin.*, **71** (4), 628–642.

——, D. Gu, B. Zheng, C. Li, and J. Zhang, 2014: Anomalous transport of water vapor for sustained torrential rain and its variation (in Chinese). *J. Trop. Meteor*, **30** (6), 1001–1010.

Liu, F., B. Wang, and I.-S. Kang, 2015: Roles of barotropic convective momentum transport in the intraseasonal oscillation. *J. Climate*, **28**, 4908–4920, https://doi.org/10.1175/JCLI-D-14-00575.1.

Liu, R., J. Sun, J. Wei, and S. Fu, 2016: Classification of persistent heavy rainfall events over South China and associated moisture source analysis. *J. Meteor. Res.*, **30**, 678–693, https://doi.org/10.1007/s13351-016-6042-x.

Ren, X., X.-Q. Yang, and X. Sun, 2013: Zonal oscillation of western Pacific subtropical high and subseasonal SST variations during Yangtze persistent heavy rainfall events. *J. Climate*, **26**, 8929–8946, https://doi.org/10.1175/JCLI-D-12-00861.1.

Reynolds, R. W., T. M. Smith, C. Liu, D. B. Chelton, K. S. Casey, and M. G. Schlax, 2007: Daily high-resolution-blended analyses for sea surface temperature. *J. Climate*, **20**, 5473–5496, https://doi.org/10.1175/2007JCLI1824.1.

Tian, S.-F., and T. Yasunari, 1998: Climatological aspects and mechanism of spring persistent rains over central China. *J. Meteor. Soc. Japan*, **76**, 57–71, https://doi.org/10.2151/jmsj1965.76.1_57.

Wan, R., and G. Wu, 2009: Temporal and spatial distributions of the spring persistent rains over southeastern China. *Acta Meteor. Sin.*, **23** (5), 598–608.

Wang, B., and X. Xie, 1997: A model for the boreal summer intraseasonal oscillation. *J. Atmos. Sci.*, **54**, 72–86, https://doi.org/10.1175/1520-0469(1997)054<0072:AMFTBS>2.0.CO;2.

——, P. Webster, K. Kikuchi, T. Yasunari, and Y. Qi, 2006: Boreal summer quasi-monthly oscillation in the global tropics. *Climate Dyn.*, **27**, 661–675, https://doi.org/10.1007/s00382-006-0163-3.

Wang, J., Z. Wen, R. Wu, and A. Lin, 2017: The impact of tropical intraseasonal oscillation on the summer rainfall increase over southern China around 1992/1993. *Climate Dyn.*, **49**, 1847–1863, https://doi.org/10.1007/s00382-016-3425-8.

Wang, M., J. Wang, and A. Duan, 2017: Propagation and mechanisms of the quasi-biweekly oscillation over the Asian summer monsoon region. *J. Meteor. Res.*, **31**, 321–335, https://doi.org/10.1007/s13351-017-6131-5.

Webster, P. J., 1983: Mechanisms of monsoon low-frequency variability: Surface hydrological effects. *J. Atmos. Sci.*, **40**, 2110–2124, https://doi.org/10.1175/1520-0469(1983)040<2110:MOMLFV>2.0.CO;2.

——, and J. R. Holton, 1982: Cross-equatorial response to middle-latitude forcing in a zonally varying basic state. *J. Atmos. Sci.*, **39**, 722–733, https://doi.org/10.1175/1520-0469(1982)039<0722:CERTML>2.0.CO;2.

Zhang, D., B. Zheng, X. Wang, C. Cun, and Y. Zhao, 2015: Preliminary research on circulation patterns in the persistent heavy rain processes during the first rainy season in South China (in Chinese). *Trans. Atmos. Sci.*, **38** (3), 310–320.

Zhang, J., L. Li, T. Zhou, and X. Xin, 2013: Evaluation of spring persistent rainfall over East Asia in CMIP3/CMIP5 AGCM simulations. *Adv. Atmos. Sci.*, **30**, 1587–1600, https://doi.org/10.1007/s00376-013-2139-7.

Zhang, Y. C., J. H. Sun, and S. M. Fu, 2017: Main energy paths and energy cascade processes of the two types of persistent heavy rainfall events over the Yangtze River–Huaiheriver basin. *Adv. Atmos. Sci.*, **34**, 129–143, https://doi.org/10.1007/s00376-016-6117-8.

Zhao, Y., D. Wang, Z. Liang, and J. Xu, 2016: Improving numerical experiments on persistent severe rainfall events in southern China using spectral nudging and filtering schemes. *Quart. J. Roy. Meteor. Soc.*, **142**, 3115–3127, https://doi.org/10.1002/qj.2892.

Zheng, B., A. Lin, J. Yuan, D. Gu, C. Li, and J. Liang, 2007: Study on the cause of Heavy Rain 200506 (HR0506) in Guangdong. *J. Trop. Meteor.*, **13** (2), 145–148.